Research
Advanced Materials and Materials Genome—Article

Individualized Pixel Synthesis and Characterization of Combinatorial Materials Chips

Xiao-Dong Xiang[1], Gang Wang[2], Xiaokun Zhang[3], Yong Xiang[3], Hong Wang[1]*

ABSTRACT Conventionally, an experimentally determined phase diagram requires studies of phase formation at a range of temperatures for each composition, which takes years of effort from multiple research groups. Combinatorial materials chip technology, featuring high-throughput synthesis and characterization, is able to determine the phase diagram of an entire composition spread of a binary or ternary system at a single temperature on one materials library, which, though significantly increasing efficiency, still requires many libraries processed at a series of temperatures in order to complete a phase diagram. In this paper, we propose a "one-chip method" to construct a complete phase diagram by individually synthesizing each pixel step by step with a progressive pulse of energy to heat at different temperatures while monitoring the phase evolution on the pixel *in situ* in real time. Repeating this process pixel by pixel throughout the whole chip allows the entire binary or ternary phase diagram to be mapped on one chip in a single experiment. The feasibility of this methodology is demonstrated in a study of a Ge-Sb-Te ternary alloy system, on which the amorphous-crystalline phase boundary is determined.

1 Introduction

Establishing the systematic relationships between materials composition, structure, synthesis parameter, and property, which are in general presented as "phase diagrams," is one of the central tasks of materials science and engineering, and remains a great challenge. Conventional materials research methodology, characterized by synthesizing and characterizing one sample at a time, is costly, time-consuming, unsystematic, and, given these disadvantages, insufficient for the current era of accelerating technology. Meanwhile, combinatorial materials chip technology, featuring high-throughput synthesis and the characterization of materials libraries containing 10^2–10^4 samples on one small substrate in a short period of time [1], has demonstrated great potential to break through the existing bottleneck. Over the past two decades, high-throughput experimental technologies have undergone rapid progress [2, 3]. A wide range of techniques and related instruments has been developed for synthesizing materials libraries of various forms (thin film [4], powder [5], bulk [6], liquid [7], etc.) and characterizing composition [8], structure [9], and electrochemical [10], catalytic [11], electromagnetic [12], magnetic [13], optical [14], thermal [15], and mechanical [16] properties.

Take the ternary equilibrium phase diagram as an example. Conventionally, an experimentally determined phase diagram requires studies of phase formation at a range of temperatures for each composition and the compilation of data in order to draw the phase boundaries in a 3-D space with a horizontal composition map and a vertical temperature axis. Often, a collection of thousands of experiments is needed, which typically takes years of effort from multiple research groups [17–21]. In contrast, a study of one temperature section of the ternary phase diagram of Fe-Co-Ni using the materials chip method was completed within a few days [22]. An equilateral-triangle-shaped thin-film materials library covering the whole range of Fe-Co-Ni compositions was annealed at 600 °C under a 10^{-8} Torr (1 Torr = 133.322 Pa) vacuum for 3 h. Structural phases were identified and the phase diagram is shown in Figure 1. This diagram agrees quite well with the reported phase diagrams constructed by conventional methods [20, 21] at this temperature, except that two new amorphous regions not included in the existing phase diagram were identified for the first time. Thus, the benefits of the high-throughput experiment approach are clearly shown.

However, significant limitations still exist in current high-throughput experimental techniques. In particular, the whole materials library is usually processed in parallel, that

is, under the same thermal conditions. Thus, with current techniques, although a materials library can cover the entire composition spread with better than 1% resolution (the equivalent of ~5000 compositions), only one isothermal section of the phase diagram can be mapped in one experiment. For example, Figure 1 shows the 600 °C isothermal section of the Fe-Co-Ni phase diagram. High-temperature phases such as δ-Fe, which is only formed at 1394 °C and is stable up to 1538 °C in the Fe-Co alloy system shown in Figure 2 [19], cannot be studied using the same chip. To map the temperature range of this Fe-Co alloy system at a 10 °C interval, 120 materials libraries are still required.
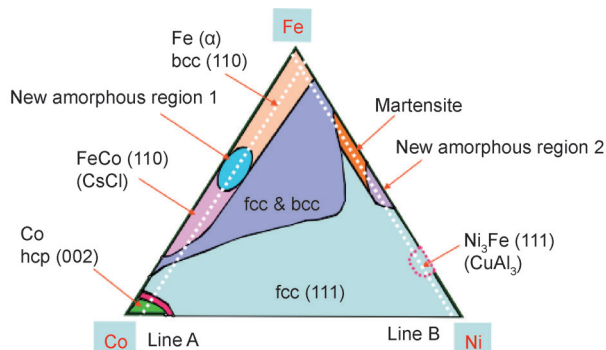

Figure 1. Fe-Co-Ni ternary phase diagram at 600 °C mapped by high-throughput approaches [22].
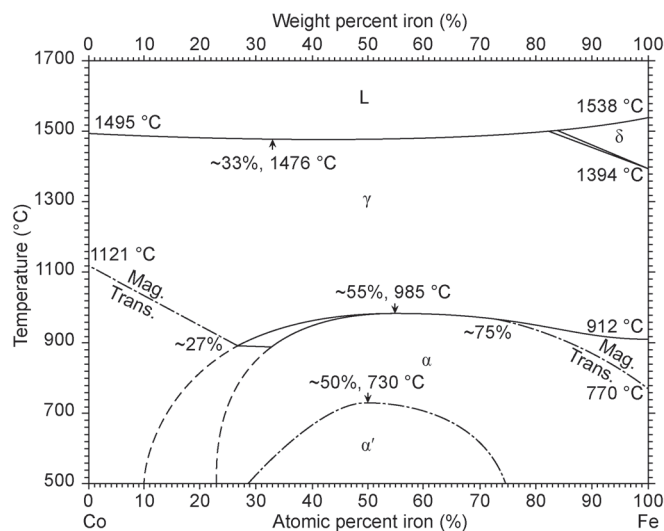

Figure 2. Classical binary phase diagram of Fe-Co alloy system [19].

For more efficient mapping of a complete phase diagram using the materials-library approach, each pixel needs to be individually processed step by step by a progressive heat-treatment procedure while the phase evolution on the pixel is monitored *in situ* in real time. The same procedure is then repeated pixel by pixel on the whole chip. This way, only one combinatorial materials library is required.

2 One-chip method

We propose here a method to construct a complete phase diagram with only one combinatorial materials library (one

chip). The workflow of the method is depicted in Figure 3. First, a thin-film materials library with designed composition distribution is deposited layer by layer, followed by thermal diffusion at relatively low temperature (a few hundred degrees Celsius) to allow complete elemental mixing throughout the thickness without the formation of any crystallized phase [23–25]. Because of the sub-micron film thickness, the mixing is confined within a pixel in the film plane. A pulsed energy beam (such as a laser or an electron beam) radiates onto each pixel sequentially to enable the phase formation on the pixel. The temperature of the processed pixel is either estimated based on heat-transfer theories or continuously measured by infrared (IR) thermometry, and the phase change during the thermal processing is monitored by an *in-situ* characterization technique in real time. For example, phase change can be detected by optical reflection, as described below in this paper, and the material structures can be monitored by high-throughput X-ray diffraction (XRD) using a synchrotron light source. The time between pulses is controlled so that there is enough time to process the characterization data, and the pulse width is managed to cause phase forming or phase transition. An interactive control system is implemented to control the thermal process according to temperature feedback or the progress of phase change.
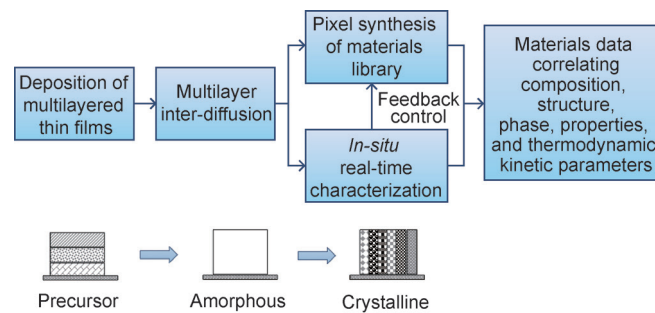

Figure 3. Workflow of pixel synthesis of combinatorial materials library with *in-situ* characterization in real time and the corresponding phase evolution of the materials library.

2.1 Deposition of multilayered thin-film precursor

To obtain a complete phase diagram, the first step is to fabricate a composition spread fully covering the compositions in the target materials system. Layered stacks of component films deposited by physical vapor deposition (PVD) methods such as ion-beam sputtering, magnetron sputtering, pulsed-laser deposition (PLD), and molecular-beam epitaxy (MBE) offer a well-controlled distribution because the composition is precisely determined by the thickness ratio between ingredient elements through a precision mask scheme. A precursor materials library covering a complete ternary composition range can be conveniently prepared using a continuously moving shutter [26]. As indicated in Figure 4(a), a ternary thin-film materials library is deposited on a triangular substrate. The shutter starts to move from one edge of the substrate toward the opposite corner at a constant speed dur-

ing the deposition of layer A, providing a wedge-shaped distribution, shown in Figure 4(b). Then the substrate is rotated 120° clockwise and is ready for the next element deposition. By repeating the process two times, the complete composition spread of a ternary materials system is fabricated (Figure 4(b)). By the same token, a binary materials library can be prepared by rotating only once by 180° on a rectangular or square substrate.
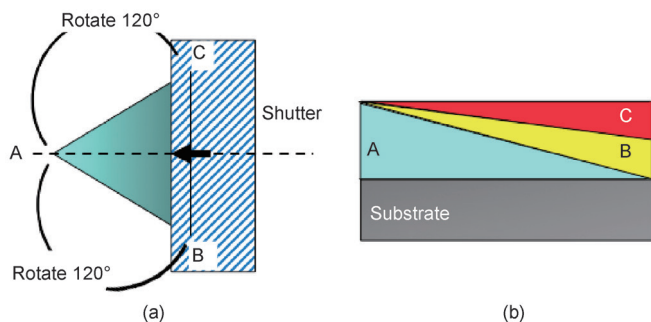

Figure 4. (a) The schematic illustration of the multilayered thin-film deposition; (b) the resultant multilayered thin films with gradient composition spread.

Figure 5 shows an ion-beam deposition (IBD) system (developed by Infinite Materials Technology Inc., China) designed to carry out the multilayered thin-film deposition process and the subsequent diffusion process (see Section 2.2) without breaking the vacuum. The system consists of five chambers: the target storage chamber, deposition chamber, annealing chamber, and two transfer chambers. The 48-slot target storage chamber is independently evacuated by a turbomolecular pump to maintain a better than 5×10^{-8} Torr vacuum to prevent the targets from contamination. In the deposition chamber, a radio-frequency (RF) ion source is used to generate an ion beam for deposition. The arrangement of target, substrate, and ion source is optimized to achieve a thickness uniformity of better than ± 3% over a 1 in × 1 in

area. An auxiliary ion source is used for substrate cleaning to improve the thin-film quality. A computer-controlled precision moving shutter is installed on the substrate stage to generate the linear gradient of the thickness of precursor thin films.

When the deposition of the multilayer thin film is completed, the substrate will be transferred to the annealing chamber for a thermal diffusion process up to 500 °C before being exposed to air.

2.2 Diffusion of the multilayered precursor

For individualized pixel synthesis to work effectively, it is important to have the precursor material well mixed at the atomic level throughout the film depth. A thermal diffusion process is employed to homogenize the multilayer precursor in the depth direction.

Fister and Johnson studied the effect of diffusion length on controlling solid-state reactions in ultrathin-film superlattice composites [27]. A solid-state reaction includes two competing steps, interdiffusion and nucleation/crystallization. The authors noted that the diffusion time is proportional to the square of the diffusion distance, which is closely related to the layer thickness. By reducing the layer thickness, it is possible to control the diffusion to complete before nucleation occurs. As a result, the interfaces disappear quickly and a homogeneous, amorphous alloy forms without nucleation. In contrast, once the layer is above a critical thickness, the composite behaves like a normal thin-film diffusion couple, in which nucleation occurs at the interfaces. The thickness dependence of the result has important implications on the design of a ternary materials library. First, the critical diffusion distances in the relevant binary diffusion couples should be predetermined. The layer sequence should also be chosen so as to suppress the occurrence of a very stable binary compound, which might hinder the formation of the ternary phase. A ternary materials library is then prepared such that
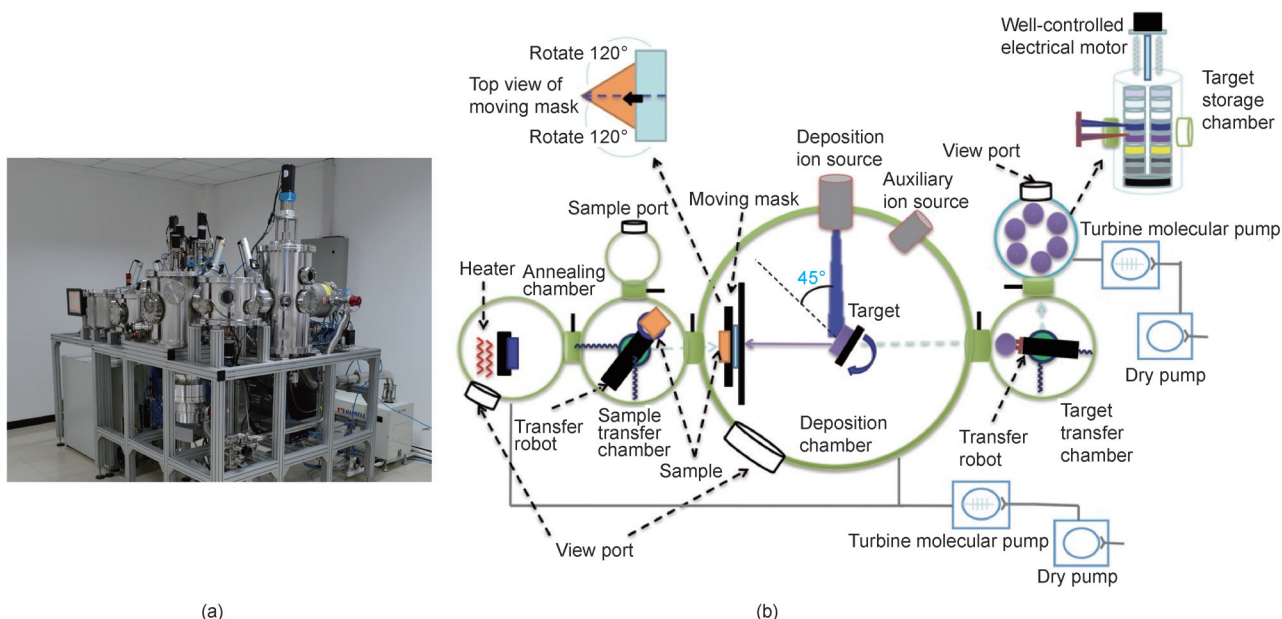

Figure 5. (a) Photograph and (b) schematics of the IBD system.

all of the diffusion distances are below the critical values to ensure a homogeneous, amorphous precursor.

Because all of the interfaces disappear during the formation of the amorphous precursor, nucleation becomes more difficult, as with the case of homogeneous nucleation. Thus, the nucleation temperature may be increased by several hundred degrees Celsius compared with the thick-film case [27]. In practice, additional process variables can be implemented to influence nucleation temperatures, such as choosing an adequate crystal structure of the substrate surface [23, 24, 28] and introducing controlled impurities as nucleation agents.

The proposed method differs from the conventional method in that the thermal process is run from low to high temperature. As indicated by the red dashed line in Figure 6, an amorphous sample will subsequently transform into thermodynamically stable phases in the corresponding temperature range when it is gradually heated, allowing the true boundary of the solid-state transition at low temperatures to be detected.
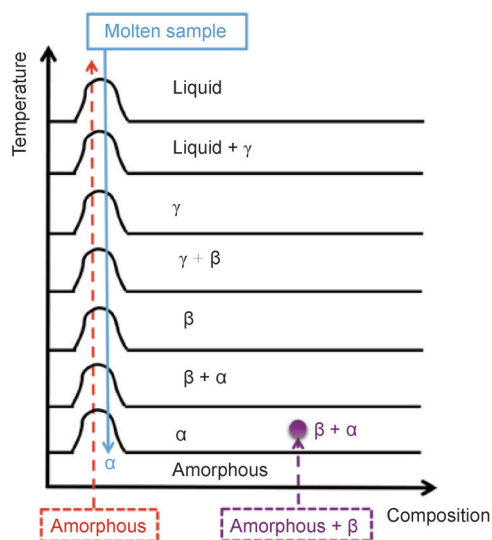

Figure 6. Schematics of the phase evolution of an amorphous sample gradually heated (red dashed line), a molten sample gradually cooled (blue line), and a partially crystallized amorphous sample gradually heated (purple dashed line).

On the contrary, in the conventional method the multi-element sample is first melted and then gradually cooled from high to low temperature. As the experimental process is mostly in equilibrium, the amorphous and crystal phase boundary cannot be identified as the temperature decreases (see the blue line in Figure 6). This explains why the two amorphous regions were marked in Figure 1 [22], but not in the conventional phase diagrams.

If the binary phases are not totally prevented at the interfaces between two layers, they will become diffusion barriers for further mass transfer. This is particularly a serious concern for the interdiffusion process between multilayers of non-metallic compounds such as oxides and nitrides [25]. Under such circumstance, a much higher temperature and longer time may be required to promote further mixing of the third precursor and the ternary phase formation. Despite

these measures, binary crystal residuals are likely to remain, which may cause complications in phase identification. Therefore, it is always preferable to prevent the precursor material from nucleating so that the materials library stays in an amorphous form after thermal diffusion. Indeed, this is not an issue in the conventional phase diagram study, because tens to hundreds of hours of soak time are used during the annealing process to satisfy the equilibrium requirements.

The temperature of diffusion/amorphization in the annealing chamber should be carefully chosen. It was demonstrated that diffusion under relatively low temperatures resulted in a well-mixed amorphous precursor layer, which is preferable because it enables the subsequent epitaxial crystallization process to occur easily at higher temperatures [23–28]. Diffusion also takes place simultaneously in the lateral direction during the process. Since the dimension of a sampling area is several orders of magnitude larger than the film thickness, the lateral homogenization will not affect the neighboring region; rather, it makes the area itself more uniform.

2.3 Pixel synthesis

As mentioned above, the well-mixed amorphous precursor of a materials library would then be synthesized by a step-by-step and pixel-by-pixel method, using an energy beam such as a pulsed laser with tunable amplitude and pulse width.

The temperature of the processed pixel is a critical parameter of the phase diagram and should therefore be carefully determined. There are two main options. First, the IR thermal radiation spectrum $r(\lambda, T)$ and the IR reflective spectrum $R(\lambda, T)$ of the same wavelength range need to be measured after each heating pulse. A fast, highly sensitive infrared spectrometer is the most desirable tool for this task. The emissivity of the surface $\varepsilon(\lambda, T)$ is described by the equation

$$\varepsilon(\lambda, T) = 1 - R(\lambda, T) \tag{1}$$

The surface temperature of the processed pixel can be deduced precisely from solving the equation

$$r(\lambda, T) = \varepsilon(\lambda, T)B_\lambda(\lambda, T) \tag{2}$$

and Planck's law of blackbody radiation

$$B_\lambda(\lambda, T) = 2hc^2\lambda^{-5}/\left(e^{hc/(\lambda K_B T)} - 1\right) \tag{3}$$

where $B_\lambda(\lambda, T)$ is the blackbody radiation spectrum at absolute temperature T; λ is wavelength; and h and c are the Planck constant and the speed of light, respectively.

Second, if thermal properties (heat capacity, density, and thermal conductivity) of the sample and substrate as well as energy-beam parameters (pulse power, pulse duration, spot size, etc.) are known, simulations can be carried out to calculate the temperature rise of the pixel under one pulse radiation. Furthermore, with the help of calibration, this calculation can be simplified with a certain level of accuracy as the equation

$$\Delta T = P_0\tau(1-R)/C_{eff} \tag{4}$$

where P_0 and τ are the laser power (amplitude) and the pulse width, respectively; R is the optical reflectivity of the pixel surface at the laser wavelength. The effective heat capacity,

C_{eff}, of the energy-beam radiated pixel is a function of the total effective thermal mass m_t, including the active thermal mass derived from the thin film and substrate, and is dependent on the pulse width (strong dependence), the amplitude (weak dependence since the specific heat capacity is temperature dependent), and other materials properties.

When the pulse width varies, the thermal mass of the processed pixel changes accordingly. A wider pulse width provides a longer time for heat to transfer to a larger volume and results in an increased thermal mass. The τ-dependent thermal mass can be simulated by commercial software based on the classical theory of heat transfer, preferably with the help of calibration for better accuracy. Considering that the spot size of the laser beam is several orders of magnitude larger than the film thickness and the scale of heat transfer, the heat transfer during one pulse can be treated by one-dimensional approximation along the depth direction, which significantly simplifies the problem.

If we keep the pulse width constant and control the heating temperature by tuning the power of the energy beam, the thermal mass of the processed pixel can be approximated as a constant, and the estimation of the heating temperature will be even simpler. However, an energy beam with tunable power requires more effort on instrumental development than the one with a tunable pulse-width.

The intrinsic fast cooling of the pulsed energy-beam processing allows the phase evolution to be captured at the temperature generated at the given heating event. In addition, after being heated to a liquid state, the pixel will return to an amorphous phase. Therefore, it is possible to align all heating events to the same starting point—the amorphous phase. The phase-evolution study of an amorphous sample heated from low temperature to high temperature is a remedy for the kinetically-controlled non-equilibrium process of the thin film. It provides a unique opportunity to understand the amorphous material's quenchability, which is of great importance for amorphous-alloy and phase-change storage applications.

2.4 *In-situ* real-time characterization of pixels

During the synthesis of one pixel in the materials library, the phase evolution after each pulse should be characterized *in situ* in real time. In principle, various characterization methods can be used to indicate phase formation, since many physical or chemical properties will change as a result. White spectrum XRD based on a synchrotron radiation light source is by far the most promising technique for direct structural characterization in real time.

For XRD to occur, the following Bragg condition must be satisfied:

$$2d\sin\theta = n\lambda \qquad (5)$$

where λ is the wavelength of the X-ray; d is the inter-planar spacing; θ is the angle between the diffracting crystal plane and the incident X-ray; and n is a positive integer. When a monochromatic X-ray shines on a polycrystalline sample with a random orientation, the diffraction will occur in different directions. To collect diffracting light, the detector must mechanically scan a wide range of θ angles, as shown

in Figure 7(a), which takes a long time. If a beam of "white" X-ray with continuous spectrum is used, in theory, a suitable wavelength that satisfies the Bragg condition always exists at any given θ, as shown in Figure 7(b). The complete diffraction pattern can be collected instantly using an energy dispersive detector without mechanical scanning.
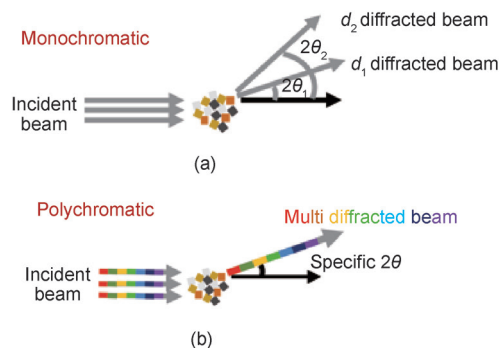

Figure 7. (a) Monochromatic X-ray powder diffraction; (b) polychromatic X-ray powder diffraction.

In the case of a single crystal or an epitaxial film sample, if the X-ray is monochromatic, the sample needs to be rotated or oscillated to satisfy the Bragg condition. However, if a polychromatic X-ray is used, the Laue diffraction pattern can be readily obtained. The entire set of diffraction spots are collected by an area detector with a one-time exposure without rotation of the sample. Figure 8 depicts single-crystal diffraction with monochromatic (left) and polychromatic (right) X-ray beams. Therefore, "white beam" XRD allows rapid determination of the crystal structure in both cases.
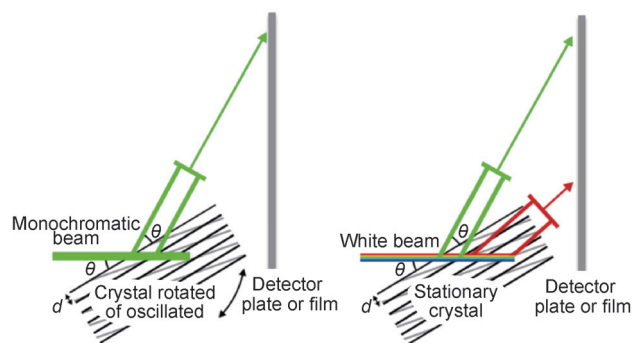

Figure 8. Monochromatic (left) and polychromatic (right) X-ray single-crystal diffraction.

Figure 9 illustrates a schematic design of the experimental setup for the "one-chip method." Each pixel on the combinatorial materials library is thermally processed step-by-step using a tunable pulsed laser beam in conjunction with a real-time feedback control mechanism. The phase change is characterized *in situ* following each heating step by polychromatic micro-beam synchrotron radiation XRD, as well as optical reflectivity. Once the preset phase boundary, such as phase transition or the pixel melting, is detected, the signal will feedback to the control system to stop heating on the pixel and the experiment will move to the next pixel.
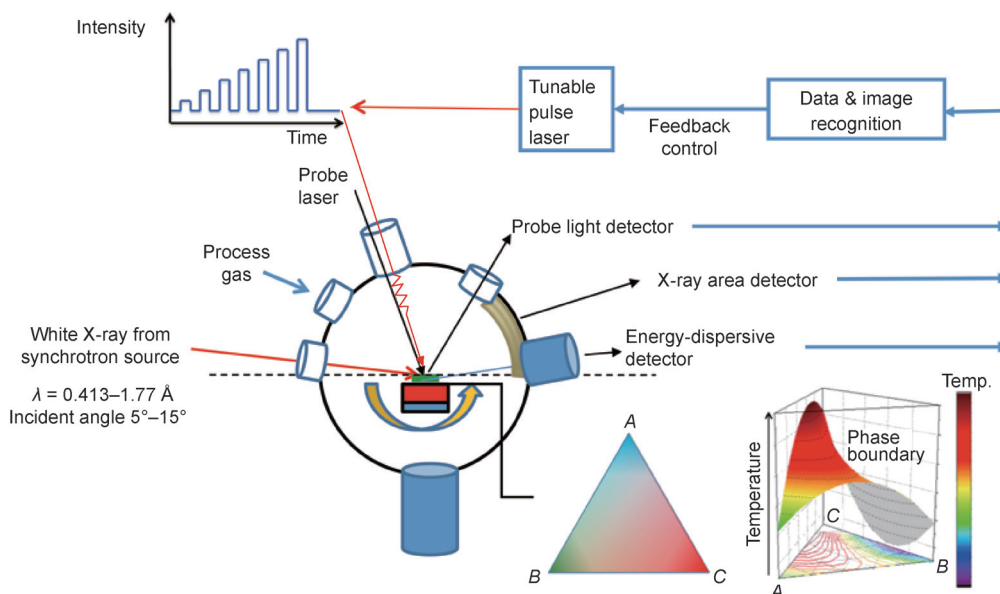
Figure 9. Schematic diagram of experimental setup for the "one-chip method" — an apparatus combining pulse laser-powered pixel synthesis with *in-situ* real-time micro-beam white XRD and optical reflectivity measurement.

The "white beam" X-ray on the left side of Figure 9 is from a synchrotron beamline such as Shanghai Synchrotron Radiation Facility (SSRF), one of whose beamlines provides energy ranging from 7 keV to 30 keV (λ = 0.413–1.77 Å). In order to cover the inter-planer spacing from 0.82 Å to 4.43 Å (equivalent to the 2θ scan from 20° to 140° for Cu Kα radiation, λ = 1.54 Å using typical lab XRD equipment), the incident angle is set between 5° and 15°. An energy dispersive detector is used to collect the powder diffraction signals, and an area detector is for Laue diffraction pattern of single crystal or epitaxial thin-film sample. In addition, a probe laser beam and a light detector are installed to monitor the phase transition of the processed pixel based on changes in optical reflectivity. Note that the heating laser beam and the probe beam should be at different wavelengths and have orthogonal polarizations to avoid interference.

While the structure is detected by white beam XRD, the composition of the pixel is measured by X-ray fluorescence (XRF). Both signals are polychromatic and are collected by the energy dispersive detector. To distinguish between the two, the energy dispersive detector needs to include two sensors installed a few degrees apart so that the signals are collected from two different angles at the same time. Since the XRD signal is angle-dependent while the XRF signal is not, the XRD can be deduced from the difference between the two data sets. The crystal structure and the composition are analyzed simultaneously using this method.

3 Pixel synthesis and characterization of phase-change materials

Phase-change materials (PCMs) hold great promise in information storage applications [29–31], and have attracted great interest in both the academic and the industrial communities [32–35]. Thin films of PCMs can undergo a relatively fast reversible transformation between the amorphous and crystalline phases, and the optical reflectivity varies significantly due to the transition. For this reason, PMCs were chosen as model materials in this study to verify the feasibility of individualized pixel synthesis and *in-situ* real-time characterization of combinatorial materials chips.

We prepared the well-mixed precursors of a systematic materials library of Ge-Sb-Te (GST) ternary alloy films using the methodology and instrument described in Section 2. A laser-pulse scanning optical microscope (LPSOM) was developed based on a traditional optical microscope with a motorized stage (Figure 10). A 40 mW diode laser was employed as the heating source, with the pulse width and power controlled by a computer. The beam was focused through the objective lens to a ~1 μm spot size at the sample surface. An autofocus control system was installed to the light path to monitor whether the objective-lens to sample-surface distance changed, and to provide a feedback signal to ensure that the system stayed in focus. This laser power heated the illuminated area with a longer pulse each time until the temperature was high enough to cause phase changing of the material. Once the material changes phase, the optical reflectivity changes correspondingly, and can be collected by the same objective lens and finally detected by the optical detector. In order to get a reflectivity image of the whole test sample, a motorized *X-Y* stage was controlled by a computer to scan over the whole library to synthesize and measure every pixel.

Figure 11 shows the timing diagram of the test system. The *X-Y* stage first move the sample to a test pixel. The autofocus is then turned on to adjust the sample surface to the focal plane. Set at a specific power level and the pulse width, the heating laser pulses is radiated onto the test pixel. During this period, the detector and autofocus are turned off to avoid interference or damage from the laser pulse. After the heat-
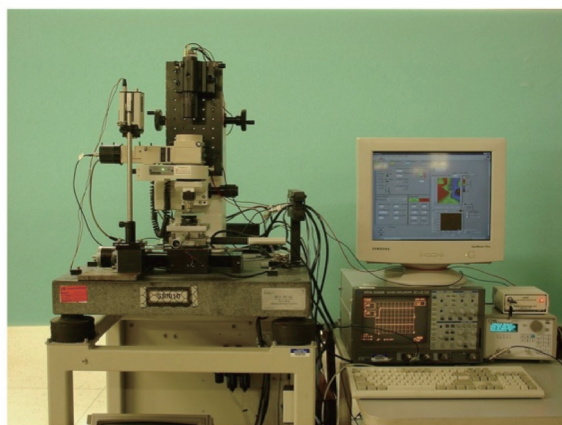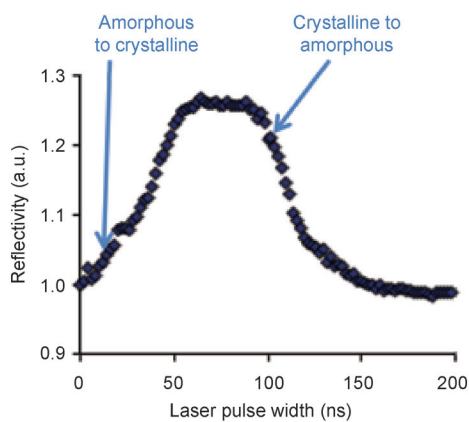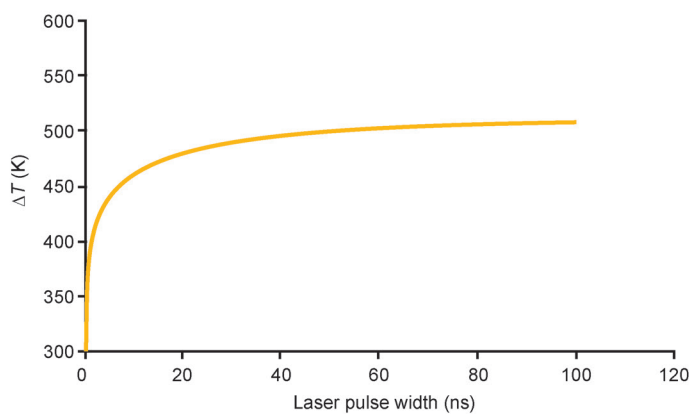
(a)
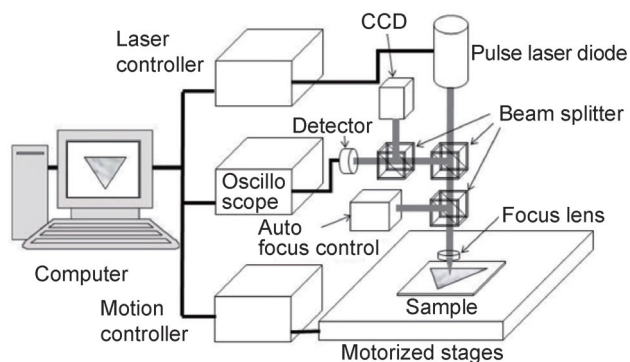
(b)

Figure 10. The (a) photo and (b) block diagram of the laser-pulse scanning optical microscope.

Figure 11. Timing diagram of the laser-pulse scanning optical microscope measurements.

ing pulse, a low-power laser pulse is generated as a detecting signal to measure the reflectivity of the treated sample, and the reflection is collected by the detector. If the reflectivity is unchanged, the next test stays at the same pixel but the pulse width is increased to raise the temperature. Usually a series of pulses are applied to the same pixel consecutively until phase change is detected. The pulse width ranges from a few nano-seconds to over 100 nano-seconds.

The temperatures of amorphous-to-crystalline and crystal-line-to-amorphous phase transitions are critical parameters of PCMs, especially for the purpose of lowering the power consumption of phase-change memories. The thermal history of a heated pixel is depicted in Figure 12(a). When the precursor is initially prepared, it is in an amorphous phase that has low reflectivity. As the heating pulse gradually increases its width, more heat is absorbed and the temperature eventually reaches the point (T_c) at which the crystalline transition occurs, leading to a significant increase in reflectivity. As the pulse width continue to increase, the temperature rises to a level enough to melt the material (the glass transition, T_g). When the laser pulse stops, the liquid is quenched into the amorphous phase again, due to the high thermal mass of the substrate as compared with the film precursor. In the end, this pulse sequence completes a full cycle of amorphous-crystalline-amorphous transformation. Continue moving the X-Y stage pixel by pixel, the time spectrum on every location is obtained. Based on this data, the crystallization temperature and the glass-transition temperature phase diagram can be mapped. Under the approximation that the temperature vs. laser pulse-width relation at different positions follows the same general trend shown in Figure 12(b), the pulse-width-dependent thermal mass of the radiated pixel is simulated by commercial software, and the $\Delta T(\tau)$ curve is calibrated using known data of the $Ge_2Sb_2Te_5$ region. The calibrated curve is used to calculate the T_c map shown in Figure 13, which is consistent with the data published in the previous literature [36–40]. The glass-transition temperature phase diagram of GST alloys separately requires much more work to analyze and will be reported in the future.

Figure 12. (a) A typical phase-transition time spectra of the GST phase-change material; (b) simulated temperature vs. laser pulse-width curve, which is calibrated by the known T_c point in the GST map.
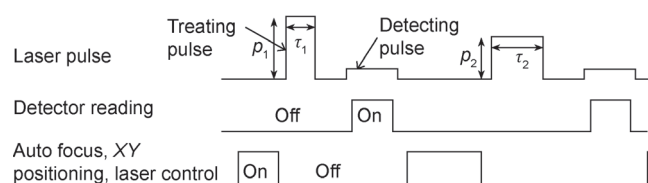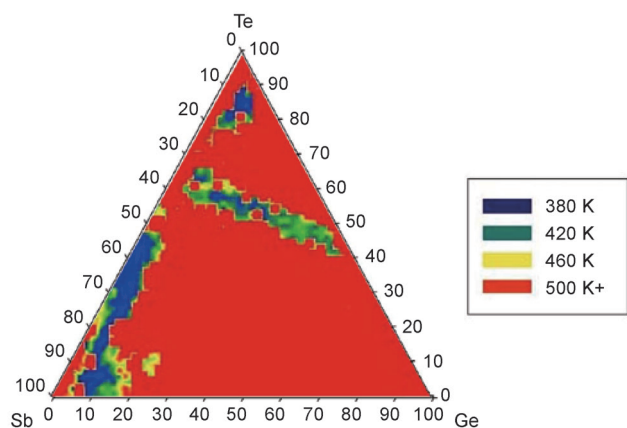
Figure 13. The amorphous-to-crystal phase-transition temperature (T_c) phase diagram of GST alloys as a function of composition.

4 Summary

In this article, we propose a new paradigm to rapidly construct a complete phase diagram using step-by-step individualized pixel synthesis and *in-situ* real-time characterization pixel by pixel throughout the combinatorial materials chip, which allows a binary or ternary phase diagram to be mapped on one chip in one single experiment. The feasibility of the "one-chip method" is demonstrated in a study of the Ge-Sb-Te ternary alloy system, on which the amorphous-crystalline phase boundary is determined; this study clearly shows the advantages of this approach. Further studies of the time-scale effect are required to correlate to conventional equilibrium phase diagrams.

Acknowledgements

Compliance with ethics guidelines

Xiao-Dong Xiang, Gang Wang, Xiaokun Zhang, Yong Xiang, and Hong Wang declare that they have no conflict of interest or financial conflicts to disclose.

References

1. X. D. Xiang, et al. A combinatorial approach to materials discovery. *Science*, 1995, 268(5218): 1738–1740

2. M. L. Green, I. Takeuchi, J. R. Hattrick-Simpers. Applications of high throughput (combinatorial) methodologies to electronic, magnetic, optical, and energy-related materials. *J. Appl. Phys.*, 2013, 113(23): 231101

3. R. A. Potyrailo, V. M. Mirsky. Combinatorial and high-throughput development of sensing materials: The first 10 years. *Chem. Rev.*, 2008, 108(2): 770–813

4. S. S. Mao. High throughput growth and characterization of thin film materials. *J. Cryst. Growth*, 2013, 379: 123–130

5. L. Chen, J. Bao, C. Gao, S. Huang, C. Liu, W. Liu. Combinatorial synthesis of insoluble oxide library from ultrafine/nano particle suspension using a drop-on-demand inkjet delivery system. *J. Comb. Chem.*, 2004, 6(5): 699–702

6. J. C. Zhao, M. R. Jackson, L. A. Peluso, L. N. Brewer. A diffusion multiple approach for the accelerated design of structural materials. *MRS Bull.*, 2002, 27(04): 324–329

7. J. Montgomery. Chemistry. High-throughput discovery of new chemical reactions. *Science*, 2011, 333(6048): 1387–1388

8. J. M. Gregoire, D. Dale, A. Kazimirov, F. J. DiSalvo, R. B. van Dover. Cosputtered composition-spread reproducibility established by high-throughput x-ray fluorescence. *J. Vac. Sci. Technol. A*, 2010, 28(5): 1279–1280

9. J. M. Gregoire, D. Dale, A. Kazimirov, F. J. DiSalvo, R. B. van Dover. High energy x-ray diffraction/x-ray fluorescence spectroscopy for high-throughput analysis of composition spread thin films. *Rev. Sci. Instrum.*, 2009, 80(12): 123905

10. E. Reddington, et al. Combinatorial electrochemistry: A highly parallel, optical screening method for discovery of better electrocatalysts. *Science*, 1998, 280(5370): 1735–1737

11. X. Liu, et al. Inkjet printing assisted synthesis of multicomponent mesoporous metal oxides for ultrafast catalyst exploration. *Nano Lett.*, 2012, 12(11): 5733–5739

12. T. Wei, X. D. Xiang, W. G. Wallace-Freedman, P. G. Schultz. Scanning tip microwave near-field microscope. *Appl. Phys. Lett.*, 1996, 68(24): 3506–3508

13. A. Oral, S. J. Bending, M. Henini. Scanning hall probe microscopy of superconductors and magnetic materials. *J. Vac. Sci. Technol. B*, 1996, 14(2): 1202–1205

14. I. Takeuchi, et al. Monolithic multichannel ultraviolet detector arrays and continuous phase evolution in $Mg_xZn_{1-x}O$ composition spreads. *J. Appl. Phys.*, 2003, 94(11): 7336–7340

15. S. Huxtable, D. G. Cahill, V. Fauconnier, J. O. White, J. C. Zhao. Thermal conductivity imaging at micrometre-scale resolution for combinatorial studies of materials. *Nat. Mater.*, 2004, 3(5): 298–301

16. H. J. Kim, J. H. Han, R. Kaiser, K. H. Oh, J. J. Vlassak. High-throughput analysis of thin-film stresses using arrays of micromachined cantilever beams. *Rev. Sci. Instrum.*, 2008, 79(4): 045112

17. C. Allibert, C. Bernard, N. Valignat, M. Dombre. Co-Cr binary system: Experimental re-determination of the phase diagram and comparison with the diagram calculated from the thermodynamic data. *J. Less Common Met.*, 1978, 59(2): 211–228

18. K. Ishida, T. Nishizawa. The Co-Cr (cobalt-chromium) system. *Bull. Alloy Phase Diagr.*, 1990, 11(4): 357–370

19. T. Nishizawa, K. Ishida. The Co-Fe (cobalt-iron) system. *Bull. Alloy Phase Diagr.*, 1984, 5(3): 250–259

20. J. C. Tedenac. Cobalt-iron-nickel. In: G. Effenberg, S. Ilyenko, eds. *Iron Systems, Part 2*. Berlin: Springer Berlin Heidelberg, 2008: 653–672

21. V. Raghavan. Co-Fe-Ni (cobalt-iron-nickel). *J. Phase Equilibria*, 1994, 15(5): 526–527

22. Y. K. Yoo, et al. Identification of amorphous phases in the Fe-Ni-Co ternary alloy system using continuous phase diagram material chips. *Intermetallics*, 2006, 14(3): 241–247

23. H. Chang, I. Takeuchi, X. D. Xiang. A low-loss composition region identified from a thin-film composition spread of $(Ba_{1-x-y}Sr_xCa_y)TiO_3$. *Appl. Phys. Lett.*, 1999, 74(8): 1165–1167

24. Y. K. Yoo, et al. Strong correlation between high-temperature electronic and low-temperature magnetic ordering in $La_{1-x}Ca_xMnO_3$ continuous phase diagram. *Phys. Rev. B*, 2001, 63(22): 224421

25. I. Takeuchi, et al. Microstructural properties of (Ba, Sr)TiO$_3$ films fabricated from BaF$_2$/SrF$_2$/TiO$_2$ amorphous multilayers using the combinatorial precursor method. *J. Appl. Phys.*, 2001, 90(5): 2474–2478

26. Y. K. Yoo, F. Duewer, H. Yang, D. Yi, J. W. Li, X. D. Xiang. Room-temperature electronic phase transitions in the continuous phase diagrams of

perovskite manganites. *Nature*, 2000, 406(6797): 704–708

27. L. Fister, D. C. Johnson. Controlling solid-state reaction mechanisms using diffusion length in ultrathin-film superlattice composites. *J. Am. Chem. Soc.*, 1992, 114(12): 4639–4644

28. I. Takeuchi, et al. Combinatorial synthesis and evaluation of epitaxial ferroelectric device libraries. *Appl. Phys. Lett.*, 1998, 73(7): 894–896

29. A. V. Kolobov. Information storage: Around the phase-change cycle. *Nat. Mater.*, 2008, 7(5): 351–353

30. G. I. Meijer. Materials science. Who wins the nonvolatile memory race? *Science*, 2008, 319(5870): 1625–1626

31. G. Atwood. Engineering. Phase-change materials for electronic memories. *Science*, 2008, 321(5886): 210–211

32. H. F. Hamann, M. O'Boyle, Y. C. Martin, M. Rooks, H. K. Wickramasinghe. Ultra-high-density phase-change storage and memory. *Nat. Mater.*, 2006, 5(5): 383–387

33. M. Wuttig, D. Lüsebrink, D. Wamwangi, W. Wełnic, M. Gillessen, R. Dronskowski. The role of vacancies and local distortions in the design of new phase-change materials. *Nat. Mater.*, 2007, 6(2): 122–128

34. C. Peng, et al. Improved thermal stability and electrical properties for Al-Sb-Te based phase-change memory. *ECS Solid State Lett.*, 2012, 1(2): 38–41

35. X. Zhou, et al. Phase transition characteristics of Al-Sb phase change materials for phase change memory application. *Appl. Phys. Lett.*, 2013, 103(7): 072114

36. M. Belhadji, N. Benameur, J. M. Saiter, J. Grenet. Application of Gibbs-Di Marzio modified equation to the Ge-Te-Sb vitreous system. *Phys. Status Solidi B*, 1997, 201(2): 377–380

37. J. Siegel, C. N. Afonso, J. Solis. Dynamics of ultrafast reversible phase transitions in GeSb films triggered by picosecond laser pulses. *Appl. Phys. Lett.*, 1999, 75(20): 3102–3104

38. H. J. Borg, et al. Phase-change media for high-numerical-aperture and blue-wavelength recording. *Jpn. J. Appl. Phys.*, 2001, 40(Part 1, 3B): 1592–1597

39. B. J. Kooi, J. Th. M. De Hosson. On the crystallization of thin films composed of $Sb_{3.6}Te$ with Ge for rewritable data storage. *J. Appl. Phys.*, 2004, 95(9): 4714–4721

40. B. J. Kooi, W. M. G. Groot, J. Th. M. De Hosson. *In situ* transmission electron microscopy study of the crystallization of $Ge_2Sb_2Te_5$. *J. Appl. Phys.*, 2004, 95(3): 924–932